CORE
Metadata, citation and similar papers at core.ac.uk
Provided by Digital.CSIC

# Modelling and characterization of Chi phase grain boundary precipitation during aging of Fe-Cr-Ni-Mo stainless steel

W. Xu[1,*], D. San Martin[2], P. E. J. Rivera Diaz del Castillo[2] and S. van der Zwaag[2]

[1]Netherlands Institute for Metals Research, Mekelweg 2, 2628 CD, Delft, The Netherlands

[2]Fundamentals of Advanced Materials Group, Faculty of Aerospace Engineering, Delft University of Technology, Klyuverweg 1, 2629 HS, Delft, The Netherlands.

(NOTE: Since 2008, David San Martín works in the National Centre for Metallurgical Research, CENIM-CSIC, Madrid, Spain, dsm@cenim.csic.es).

*Corresponding author. Tel.: +0031 15 278 5218; Fax: +0031 15 278 4472. E-mail address: w.xu@nimr.nl. Postal address: 1.33NB, Kluyverweg 1, 2629 HS, Delft, the Netherlands.

## Abstract

High molybdenum stainless steels may contain the Chi precipitate ($\chi$, $Fe_{36}Cr_{12}Mo_{10}$) which may lead to undesirable effects on strength, toughness and corrosion resistance. In the present work, specimens of a 12Cr-9Ni-4Mo wt% steel are heat treated at different temperatures and times, and the average particle size and particle size distribution of Chi precipitate are studied quantitatively. A computer model based on

the KWN framework has been developed to describe the evolution of Chi precipitation. The kinetic model takes the natural advantages of the KWN model to describe the precipitate particle size distribution, and is coupled with the thermodynamic software ThermoCalc® for calculating the instantaneous local thermodynamic equilibrium condition at the interface and the driving force for nucleation. A modified version of Zener's theory accounting for capillarity effects at early growth stages is implemented in this model. The prediction of the model is compared to experimental results and both the average particle size and the particle size distribution are found to be in good agreement with experimental observations.

**Keywords**: Chi precipitate, Precipitation kinetics, Particle size distribution, Modelling, Stainless steel

## Introduction

Low-carbon high-alloy steels, commonly employed in aerospace and tooling applications, require a good compromise between high strength and fracture toughness. These grades are usually strengthened by intermetallic second-phase particles to achieve such compromise. The presence of Mo and Cr in the composition of these steels, can lead to the formation of Chi phase ($\chi$, $Fe_{36}Cr_{12}Mo_{12}$) after heat treatment, particularly on the grain boundaries, coherent and incoherent twin boundaries and on dislocations within the matrix [1]. The precipitation of this phase at grain boundaries depletes the local chromium content to an extent that can lead to intergranular corrosion. It has also a reverse effect on the toughness and creep ductility properties [2-4]. Moreover, recent

experimental studies show that in maraging steels, the depletion of solute in the matrix alters the stability of austenite, which affects its transformation to martensite [5].

Several investigations have reported Chi phase precipitation during isothermal heat treatment for a variety of steel grades. Most of these address the characterisation of Chi phase and its effects on the alloy mechanical and magnetic properties [2-4, 6-8]. As far as the authors are aware, a quantitative analysis of Chi precipitation kinetics is not available. This is of great importance as the presence, location, size and size distribution of the Chi particles will have a significant effect on the final steel properties. From a metallurgical standpoint, the aim of this investigation is to study the kinetics of Chi precipitation from austenite in an Fe-Cr-Ni-Mo alloy, and to establish a quantitative relationship with its heat treatment conditions.

The study of Chi precipitation requires a suitable modelling framework for capturing the complexity of the quaternary system. It is common to deal with precipitation from a supersaturated solution as the sequence of nucleation, growth and coarsening processes which are modelled separately [9, 10]. Langer and Schwartz have embedded the three processes within a model referred to as MLS [11]. More recently, Kampmann and Wagner produced a numerical approach (KWN model) [12, 13] capable to describe the particle size distribution (PSD) in the time domain, while dealing with nucleation-growth-coarsening phenomena within the same formulation. A few models based on this framework have been applied to a number of systems [14-17]. An important limitation in those approaches is that the overall kinetics is computed by imposing a constant concentration at the precipitate/matrix interface, and by employing a driving

force obtained from binary dilute solution approximation. Because of the decrease of solute supersaturation in the matrix during precipitation, the local equilibrium concentration at the precipitate/matrix interface may change significantly. Moreover, the chemical free energy change during nucleation based on the dilute solution approximation in high-alloy systems is also not precise, especially for ternary or higher order systems. The model presented here intends to overcome this problem via computing thermodynamic equilibrium in the time domain to obtain the instantaneous local equilibrium condition at the matrix/precipitate interface during precipitation. The instantaneous driving force for nucleation is calculated from ThermoCalc® [18]. A master-slave computation of KWN kinetics combined with ThermoCalc thermodynamic computation is therefore performed at every time step. A further improvement in the present computation is the incorporation of capillarity effects at early growth stages via employing a modified version of Zener's theory of precipitate growth [19, 20]. The result of this model shows good agreement with the experimental observations.

## Experimental procedures

### *Alloy composition*

The composition of the steel studied in this work is shown in Table 1. The as-received material was delivered as strips of 31x0.5 mm in thickness. The initial microstructure consists of austenite and Chi phase [21].

*Heat treatment*

The heat treatments were performed using an Adamel Lhomargy DT1000 high-resolution dilatometer [22]. Specimens were heated to 1100 ºC for 300 and 1800 s in order to dissolve all precipitates, then cooled down at 50 ºC/s to 900 ºC and held for different times (120, 300, 900, 1800 and 3600 s) to study the precipitation kinetics, and were then cooled down to room temperature at 50 ºC/s. Samples of 5 mm in width and 12 mm in length were used. To study the late stage of coarsening, a section of the sample treated for 1800 s at 1100 $^{o}$C, aged at 900 ºC for 3600 s and cooled down to room temperature, was reheated to 900 ºC for another 13 hours and subsequently water quenched.

*Microstructure examination*

For the metallographic characterization, the specimens were mounted in bakelite, ground and polished in different lap clothes (finishing with 1 µm diamond paste). A variation of Villela's mixed-acid etch [23, 24] (3 parts HCl, 2 parts $HNO_3$ and 1 part $H_2O$) was used to disclose the Chi phase by optical microscopy. The SEM analysis was carried on JEOL JSM-840A microscope with the same etching solution. The two-dimensional quantitative measurement of the radius of the Chi phase was performed using an image analyzer. An estimation of the three-dimensional radius of the Chi phase was done following the method of Hull and Houk [25].

## Experimental Results

Figure 1 (a) and (b) show representative optical micrographs of the specimen homogenised at 1100 $^{o}$C for 300 and 1800 s, respectively. After homogenisation, samples were aged to induce enough precipitation at grain boundaries so as to be revealed by chemical etching using Villela's mixed acid. It should be mentioned that austenite grain growth at 900 $^{o}$C for periods up to 3600 s is almost negligible. Thus the grain size can be considered to be constant during aging. From these micrographs it is clear that the average size of the grain after 1800 s homogenisation treatment is bigger than the sample subjected to 300 seconds treatment: 107 and 43 μm, respectively.

Figure 2 a)-c) show the microstructure of the specimen aged at 900 $^{o}$C for 300, 1800 and 3600 s after homogenisation. They show that Chi precipitates are mostly present at the austenite grain boundaries. The growth rate is appreciated from comparing these figures. Figure 2d) is an SEM image of the specimen after 14 hours aging. It shows that the coarsened Chi precipitate appears both at the grain boundaries and within the grains. The precipitates located at the grain boundaries are much bigger than those inside the grains. Next to the grain boundaries, precipitate free zones are appreciated. Within the grain, the small precipitate particles appear to be homogeneously distributed. The average size of the grain boundary particles for different aging times was estimated using an image analyzer (Table 2).

The microstructures of the specimens homogenised for 300 s at 1100 $^{o}$C and further aged for different times are shown in Figure 3. As the average grain size is small, more

grain boundaries stimulate precipitate nucleation, leading to a higher number density of particles. Moreover, the average precipitate size is smaller as compared to the 1800 s homogenisation treatment shown in Table 2.

## Model

Based on the classical nucleation theory and a modified version of Zener's theory of precipitate growth, a KWN-based numerical framework was developed. The kinetic computations were coupled to ThermoCalc® software [18] employing the TCFE3 [26] thermodynamic database and the MOB2 [27] mobility database. The time evolution of the Chi precipitate particles was computed in discreet time steps. The particle size distribution is divided into a series of discrete size classes, each represented by a control volume. In every time step, the following computations are performed: 1) An instantaneous value of the matrix supersaturation is obtained from ThermoCalc following a phase equilibrium computation; 2) nucleation is modelled by determining the number of new nuclei appearing in the class and characterized by a critical radius $r^*$ and composition $c^{\chi\gamma}$, the number of particles is then updated; 3) the growth rate of the existing particles within the spatial boundary of the control volume is obtained accounting for capillarity effects; 4) the transport of particles between every control volume is calculated via a discretisation of the continuity equation for the particle number, updating the volume fraction of the Chi precipitates; 5) mass balance is imposed assuming the matrix composition to be homogenous. Each of these computations is outlined next.

*Phase equilibrium (1)*

Thermodynamic computations are performed to obtain the instantaneous local equilibrium composition of the precipitate/matrix interface using ThermoCalc with the TCFE3 database. This produces the solute concentration in the matrix (γ) in equilibrium with the precipitate Chi (χ), $c^{\gamma\chi}$, and the solute concentration of χ precipitates in equilibrium with the matrix (γ), $c^{\chi\gamma}$. In addition, the chemical potentials of all the components are obtained and employed to determine the chemical driving force for the nucleation of the precipitates. The diffusivity pre-exponential factor $D_0$ and the activation energy $Q$ for diffusion are obtained from the mobility database MOB2.

*Nucleation (2)*

The steady state nucleation rate is obtained from [28],

$$I = \frac{dN}{dt} = N_0 \frac{kT}{h} \exp\left[\frac{-\left(\lambda_1 G^* + Q^*\right)}{kT}\right] \tag{1}$$

where $N_0$ is the initial density of nucleation sites, $Q^*$ is the activation energy for the transfer of atoms across the interface (taken to be equal to the activation energy for Molybdenum diffusion, $Q$), $k$ is the Boltzmann constant, $h$ is the Planck's constant, $G^*$ is the free energy required to overcome the barrier for nucleation and $\lambda_1$ is a scaling factor used for compensating the overestimated value for $G^*$ [29-31]. The activation energy $G^*$ for a spherical nucleus is given by

$$G^* = \frac{16\pi}{3} \frac{\sigma^3}{\Delta G_V^2} \tag{2}$$

where $\sigma$ is the precipitate/matrix interfacial energy per unit area and $\Delta G_V$ is the chemical free energy change per unit volume.

By denoting $\mu_k^\gamma$ as the $k$ component chemical potential of pure metastable austenite, $\mu_k$ as the equilibrium chemical potential of the $k$ component in Chi and $C_k^{\chi\gamma}$ as the equilibrium composition of the Chi precipitate, the molar driving force for nucleation, $\Delta G_m$, can be obtained from the dot product,

$$\Delta G_m = C_k^{\chi\gamma} \cdot \mu_k^\gamma - C_k^{\chi\gamma} \cdot \mu_k = C_k^{\chi\gamma} \cdot (\mu_k^\gamma - \mu_k) \quad (3)$$

$\Delta G_V$ is thus approximated by dividing $\Delta G_m$ by the precipitate molar volume.

The critical radius of the nucleus accounting for capillarity effects is obtained from [20]

$$\rho_c = \frac{2c^{\gamma\chi}\Gamma}{\bar{c} - c^{\gamma\chi}} \quad (4)$$

where $\Gamma$ is the capillarity constant given by the regular solution approximation,

$$\Gamma = (\frac{\sigma v^\chi}{kT})(\frac{1 - c^{\gamma\chi}}{c^{\chi\gamma} - c^{\gamma\chi}}) \quad (5)$$

where $\sigma$ is the interfacial energy per unit area and $v^\chi$ is the volume per atom in the Chi precipitate phase.

*Particle growth rate (3)*

The modelling of precipitate growth with local equilibrium at the interface is based on the theory for spherical precipitates by Zener [32], and later extended by Rivera and

Bhadeshia [19, 20] to approximately account for capillarity effects. The development of the radius of the spherical precipitate is assumed to follow the parabolic equation

$$\rho = \alpha \cdot (Dt)^{1/2} \tag{6}$$

where $\alpha$ is a dimensionless growth parameter and $D$ is the diffusion coefficient of Molybdenum.

At a radius $r$, which origin is located at the centre of the particle, the concentration field can be described as

$$c\{t,r\} = \bar{c} + [(c^{\gamma\alpha} + \frac{2c^{\gamma\alpha}\Gamma}{\rho}) - \bar{c}]\phi\{\frac{r}{(Dt)^{1/2}}\} / \phi\{\alpha\} \tag{7}$$

Where $\bar{c}$ is the average solute concentration in the matrix and

$$\phi\{\alpha\} = \frac{1}{\alpha}\exp\left\{-\frac{\alpha^2}{4}\right\} - \frac{\pi^{1/2}}{2}\operatorname{erfc}\left\{\frac{\alpha}{2}\right\} \tag{8}$$

The rate at which solute is incorporated into the growing precipitate must be equal to that arriving by diffusion to the interface, therefore

$$v[c^{\alpha\gamma} - (c^{\gamma\alpha} + \frac{2c^{\gamma\alpha}\Gamma}{\rho})] = D\frac{\partial c}{\partial r}\Big|_{r=\rho} \tag{9}$$

the expression for the particle growth rate $v$ can be obtained from

$$v\{r,t\} = \frac{\partial \rho}{\partial t} = -\frac{2D\sqrt{Dt}(2c^{\gamma\alpha}\Gamma - \bar{c}r + c^{\gamma\alpha}r)}{r(2c^{\gamma\alpha}\Gamma + c^{\gamma\alpha}r - c^{\alpha\gamma}r)[-2\sqrt{Dt} + \sqrt{\pi}re^{r^2/4Dt}\operatorname{erfc}(r/2\sqrt{Dt})]} \tag{10}$$

The diffusion coefficient $D$ is calculated from $D = D_0 \exp(-\lambda_2 Q / RT)$, where $D_0$ and $Q$ are obtained from the ThermoCalc mobility database MOB2. Due to the fact that precipitation occurs at the grain boundaries, the growth is not controlled only by bulk

diffusion. The parameter $\lambda_2$ ($0.6<\lambda_2<1$) reflects the contribution of the faster grain boundary diffusivity on the growth kinetics of the Chi precipitates. A value of $\lambda_2$=0.4-0.8 is commonly taken for grain boundary diffusion [33-35].

*Transport of particles (4)*

Analogous to the diffusion problem, the growth or dissolution of particles that occur during a time increment $\Delta t$ can be regarded as a flux of matter in or out of the control volume. The mass balance hence gives

$$\frac{\partial N_i}{\partial t} = -\frac{\partial N_i v_i}{\partial r} + S \tag{11}$$

where $N_i$ is the number density of particles of the $i^{th}$ particle size group, $v_i$ is the particle growth rate within $i$ and $S$ is the nucleation rate.

The volume fraction of Chi phase can now be calculated as

$$f_\chi = \sum_i N_i \frac{4}{3}\pi r_i^3 \tag{12}$$

Where $r_i$ is the radius of the particles in the $i^{th}$ group.

*Mass balance (5)*

The mean solute concentration in the matrix is updated from

$$\bar{C} = C_0 - (C_p - \bar{C})\int_0^\infty \frac{4}{3}\pi r^3 \phi dr \tag{13}$$

where $\phi$ is the size distribution function.

*Input values*

The model is applied to simulate the Chi precipitate evolution in a multicomponent alloy system which composition is simplified to 12Cr-9Ni-4Mo wt.% with Fe to balance. The initial equilibrium interface condition at 900 $^{o}$C is obtained from ThermoCalc and shown in Table 3. Being that the diffusivities of Cr, Mo and Ni in austenite are approximately equal, and that Mo possesses the biggest compositional gradient at the interface, this element is chosen as rate controlling for Chi growth rate (equation (10)). The Chi precipitate particles are considered to be distributed in the range of 2 nm to 2 μm, and this range is discretized to 500 size groups. Equation (11) is discretized with a forward Euler scheme for time and first order upwind schemes in space. Therefore, the time step for the $n^{th}$ calculation is chosen from the stabilization condition,

$$\Delta t^n \leq \Delta t_{CFL} = \frac{CFL \cdot \Delta x}{\left|\max v(x,t^n)\right|} \tag{14}$$

where CFL number is chosen as 0.9 and $\Delta x$ denotes the mesh width, given by $\Delta x = l / N = (2000-2)/500 = 3.996$ nm. The parameter 'max $v(x,t^n)$' is the maximum value for all the growth rates in different control volumes at a time $t^n$. In order to prevent excessively large time steps, if $\Delta t > 1$ as provided by equation (14), a value of $\Delta t = 1$ was taken. For the sake of reducing computation time, the ThermoCalc equilibrium calculations are performed for every time in the first 1000 steps and then every 100 steps; but if $\Delta t^n$ >0.01 s, they are performed every step.

The interfacial energy of precipitates in steel is usually within the range of 0.1-0.5 J/m$^2$, but no value for the Chi phase was found in the literature. The interfacial energy is assumed to be 0.1 J/m$^2$ in this calculation. The factor $\lambda_1$ is taken as 0.0015 [30, 31]. Given that the Chi precipitates are mostly found at the grain boundaries, the initial density of nucleation sites should reflect the overall grain boundary surface per unit volume and hence the grain size. The obtained average grain sizes after 1800 and 300 s homogenisation treatment were 107 μm and 43 μm (hereafter referred as Case A and B, respectively), and the chosen initial density of nucleation sites is 0.4*10$^{18}$ and 10$^{18}$ /m$^3$ respectively (inversely proportional to the average grain size). The factor $\lambda_2$ is chosen the value of 0.75 and employed for both cases. $N_0$ and $\lambda_2$ are parameters fitting the experimental measurements.

**Results and discussionF**

Figure 4 shows the particle size evolution of Chi precipitate during aging at 900 $^{o}$C for up to 7200 seconds. The empty squares and circles show the calculated progress of average particle radius. The dashed curves show the critical radius of the new nuclei formed in each time step, as obtained from equation (4); this also defines the critical size separating particles under growth or dissolution Figure 4 shows that at the early aging stage, the critical particle size increases very slowly because the volume fraction of the Chi precipitate is small and the matrix supersaturation is high enough to have insignificant effects on the nuclei size. Meanwhile, for the existing particles, the solution supersaturation and limited amount of the particles also lead to the 'free' growth of the particles in the absence of soft-impingement effects. Therefore, the

average radius of Chi particles has a fast increase at this stage. The predicted evolution of particle number density as a function of time is plotted in Figure 5. It shows that the number density of particles increases rapidly from the beginning because of the high nucleation rate, the very slow dissolution kinetics and the accumulation of the particles. Because of both the fast increase of the particle size and the high number density of particles, the volume fraction increases abruptly in this stage, as shown in Figure 6.

As result of the fast solute depletion, after about 20 seconds, the solid solution concentration in the matrix decreases significantly and therefore the critical radius of new nuclei starts to increase faster; the nucleation rate decreases to a very low value; and the total number of particles remains at a certain level (Figure 4 and Figure 5). As the volume fraction gets close to the equilibrium condition at this stage, the limited solid solution supersaturation suppresses the growth and consequently the growth rate of average particle radius decreases.

In the next stage, the coarsening mechanism starts to dominate the process in terms of big precipitates growing at the expense of smaller ones. The critical radius for nucleation approaches the mean particle radius, and they increase together with time (Figure 4). The total number of particles decreases while the volume fraction keeps close to the equilibrium level (Figure 5 and Figure 6). The computations show that the overall precipitation kinetics switches smoothly from the nucleation-growth dominated regime to growth-coarsening dominated regime without artificial separation of these three processes, this is a feature of the KWN model.

The model is applied to two initial austenite grain sizes (A and B) by means of assuming a different initial density of nucleation sites $N_0$. Figure 4 shows that there is not much difference in the average and critical particle size between the two cases at the beginning of the precipitation process, while meantime, the number density of the particles is much higher in case B because of the higher nucleation rate, as shown in Figure 5. Consequently, the volume fraction of Chi phase also increases faster in case B (Figure 6) and the volume fraction of Chi phase also gets close to equilibrium fraction at an earlier time, but with smaller average particle size. This is also the reason why the critical radius starts to increase also at an earlier time in case B. Eventually, at later stages (>2000s), and due to the faster coarsening process in case B, the number density of particles and the average size of particles reach a similar value in both cases (A and B), as indicated in Figure 4 and Figure 5.

The model allows tracing the particle size distribution throughout the whole evolution process. The predicted particle size distributions of both cases A and B are plotted in Figure 7 (a) and (b), after 300, 1800 and 3600 seconds aging corresponding, respectively, to the points marked 1-3 and character $\alpha, \beta, \chi$ in mean particle radius curve in Figure 4. The statistical results of the experimental observation are also plotted in Figure 7 as histogram for comparison with the simulation. At 120 s, the particle size distribution is characterized by a sharp peak around the average particle radius. For longer aging times, the position of this peak switches to right reflecting the increase in the mean particle size. The width of the peak increases and its height decreases due to both the lower values in total particle number and the growth/dissolution kinetics. It is

worth noting that the distribution is the natural output of the KWN model and is not the result of an assumption.

The experimental results of the average particle radius shown in Table 2 are plotted as solid squares and circles with error bars in Figure 4, showing that the simulation results are in good agreement with the experimental observations. It should be noticed that only the precipitates at grain boundaries have been taken into account in estimating the experimental average particle size. This is because, although the intragranular precipitate may be formed at the very beginning of ageing, the growth of intragranular precipitate is very slow compared to intergranular ones due to slow bulk diffusivities. Therefore, the intragranular precipitates are too small to be distinguished by SEM at the aging time we investigated. However, the existence of the precipitation within the matrix can be proven by Figure 2d) in which Chi precipitate has reached a significant size due to long time aging. The region with the larger Chi precipitates, which includes both grain boundaries and precipitate free zones next to them, as shown in Figure 2d), can be treated as an independent system. In this area, the diffusivity is much faster than the bulk diffusion and intergranular precipitates consume most of the solute in solid solutions in the matrix. For the short aging times at which the model is applied, the slow bulk diffusion has not significantly affected the fast grain boundary precipitation kinetics. But for very long time aging or precipitate evolution in the service period, the model should be modified to consider the cross effects of the intergranular and intragranular precipitates to obtain the overall precipitation kinetics.

## Conclusion

The kinetics of Chi precipitate aging at 900 $^{o}$C has been experimentally investigated. For the specimens aged up to 1 hour, the Chi precipitate is mostly found at the grain boundaries under SEM observation, while after 14 hours aging, there are both big, discontinuous precipitates at the grain boundaries and small homogenously distributed precipitates inside the grains. Next to the grain boundaries, there are precipitate free zones.

A model describing the precipitation kinetics is developed. The model is based on a KWN framework with a growth rate computation incorporating capillarity effects; the model is coupled with ThermoCalc thermodynamic databases for obtaining the instantaneous equilibrium condition at interface, the driving force for nucleation and the solution diffusions. The model is able to predict the overlapped nucleation-growth-coarsening kinetics in a natural way and trace the particle size distribution throughout the process.

The model is applied to describe the Chi precipitation kinetics at the grain boundary depletion zones. The grain boundary zones can be treated as an independent system. The predicted evolution of Chi precipitate for different heat treatments is in good agreement with the experimental observations.

**Acknowledgements**

The authors are grateful to the Netherlands Institute for Metals Research (NIMR) for the provision of funding through the programme “Designing ultra high strength corrosion resistance steels for aerospace applications” (project number MC5.04192) and “Tailoring of processable metastable steels” (project number 02EMM30-3). The authors are very grateful to Javier Vara for experimental support.

**Reference**

[1] A. F. Padilha, P. R. Rios, ISIJ International 42 (2002) 325.

[2] H. L. Cao, S. Hertzman, W. B. Hutchison, in: Stainless Steel '87, 1988, p. 151.

[3] J. K. Lai, J. R. Haigh, Weld J. 58 (1979) 1s.

[4] J. O. Nilsson, A. Wilson, B. Josefsson, T. Thorvaldsson, in: Stainless Steel '92, vol 1, 1992, p. 280.

[5] K. Aarts, D. San Marten, P. E. J. Rivera-Diaz-del-Castillo, S. van der Zwaag, Unpublished work.

[6] A. Redjaimia, A. Proult, P. Donnadieu, J. P. Morniroli, Journal of Materials Science 39 (2004) 2317-2386.

[7] C. Zakine, C. Prioul, D. Francois, Journal of Nuclear Materials 230 (1996) 78-83.

[8] J. K. Lai, C. H. Shek, Y. Z. Shao, A. B. Pakhomov, Materials Science and Engineering A 379 (2004) 308-312.

[9] J. D. Robson, H. K. D. H. Bhadeshia, Materials Science and Technology 13 (1997) 640-644.

[10] J. D. Robson, H. K. D. H. Bhadeshia, Materials Science and Technology 13 (1997) 631-639.

[11] J. S. Langer, A. J. Schwartz, J. Phys. Rev. A 21 (1980) 948.

[12] R. Kampmann, R. Wagner, Decomposition of alloys: the early stage, Oxford: Ppergamon Press, 1984, p. 91.

[13] R. Kampmann, R. Wagner, Materials Science and Technology - A comprehensive treatment, VCH, Weinheim, 1991, p. 21.

[14] J. D. Robson, M. J. Jones, P. B. Prangnell, Acta Materialia 51 (2003) 1453-1468.

[15] O. R. Myhr, Ø. Grong, Acta Materialia 48 (2000) 1605-1615.

[16] J. D. Robson, Acta Materialia 52 (2004) 4669-4676.

[17] J. D. Robson, Materials Science and Technology 20 (2004) 441-448.

[18] J. Ö. Andersson, T. Helander, L. Höglund, P. Shi, Calphad 26 (2002) 273.

[19] P. E. J. Rivera-Diaz-del-Castillo, S. van der Zwaag, in: Proceedings of the international conference on solid-solid phase transforation in inorganic materials, vol 2, TMS, Arizona, 2005, p. 381.

[20] P. E. J. Rivera-Diaz-del-Castillo, H. K. D. H. Bhadeshia, Materials Science and Technology 17 (2001) 30.

[21] D. San Martin, N. van Dijk, E. Bruck, S. van der Zwaag, Mater. Sci. Forum 500-501 (2005) 339.

[22] F. G. Caballero, C. Capdevila, C. García de Andrés, Metall. and Mater. Trans. A 32A (2001) 1283.

[23] V. Voort, Metallography, Principles and Practice, McGraw-Hill, USA, 1984.

[24] D. San Martin, P. E. J. Rivera Díaz del Castillo, E. Peekstok, S. van der Zwaag, Materials Characterization In press (2006).

[25] F. C. Hull, W. J. Houk, Journal of Metals (1953) 565.

[26] TCFE3-Thermo-Calc Steels/Fe-Alloys Database (Version 3.0, 2002), in: Royal Institute of Technology, foundation of computational thermo-dynamics, Stockholm/Sweden.

[27] MOB2, Mobility database (v2.0, 1999), in: Royal Institute of Technology, foundation of computational thermo-dynamics, Stockholm/Sweden.

[28] J. W. Christian, Theory of transformation in metals and alloys, Part I, Pergamon, Oxford, England, 1975, p. 181, 418.

[29] S. E. Offerman, N. H. van Dijk, J. Sietsma, S. Grigull, E. M. Lauridsen, L. Marguiles, H. F. Poulsen, M. T. Rekveldt, S. van der Zwaag, Science (2002) 1003.

[30] W. Xu, P. E. J. Rivera Diaz del Castillo, S. van der Zwaag, ISIJ International 45 (2005) 380.

[31] P. E. J. Rivera Diaz del Castillo, S. van der Zwaag, Metallurgical and Materials Transactions A 35A (2004) 425.

[32] C. J. Zener, J. Appl. Phys 20 (1949) 950.

[33] Y. Mishin, C. Herzig, Materials Science and Engineering A 260 (1999) 55-71.

[34] A. M. Brown, M. F. Ashby, Acta Metallurgica 28 (1980) 1085-1101.

[35] J. Fridberg, L. E. Torndahl, M. Hillert, Jernkontorets Ann 153 (1969) 263-276.

Table 1 Chemical composition of the studied steel [wt. %]

| Cr | Ni | Mo | Cu | Ti | Al | Si | C, N |
|---|---|---|---|---|---|---|---|
| 12.0 | 9.0 | 4.0 | 2.0 | 0.9 | 0.3 | 0.3 | < 0.01 |

Table 2 Chi average particle size for different aging times. A and B refer to the specimen homogenised at 1100 $^{o}$C for 1800 and 300 s, respectively

| Time (s) | 120 | 300 | 900 | 1800 | 3600 |
|---|---|---|---|---|---|
| A (μm) | 0.198±0.0493 | 0.211±0.0436 | 0.237±0.0210 | 0.264±0.0211 | 0.310±0.0214 |
| B (μm) | 0.144±0.0300 | 0.164±0.0295 | 0.207±0.0423 | 0.216±0.0270 | 0.271±0.0364 |

Table 3 The initial interface equlibrium compostion at 900 $^{o}$C

| Weight fraction | Cr | Mo | Ni | Fe |
|---|---|---|---|---|
| Alloy | 0.1200 | 0.0400 | 0.0900 | Balance |
| Austenite | 0.1185 | 0.0356 | 0.0915 | Balance |
| Chi phase | 0.1800 | 0.2114 | 0.0294 | Balance |

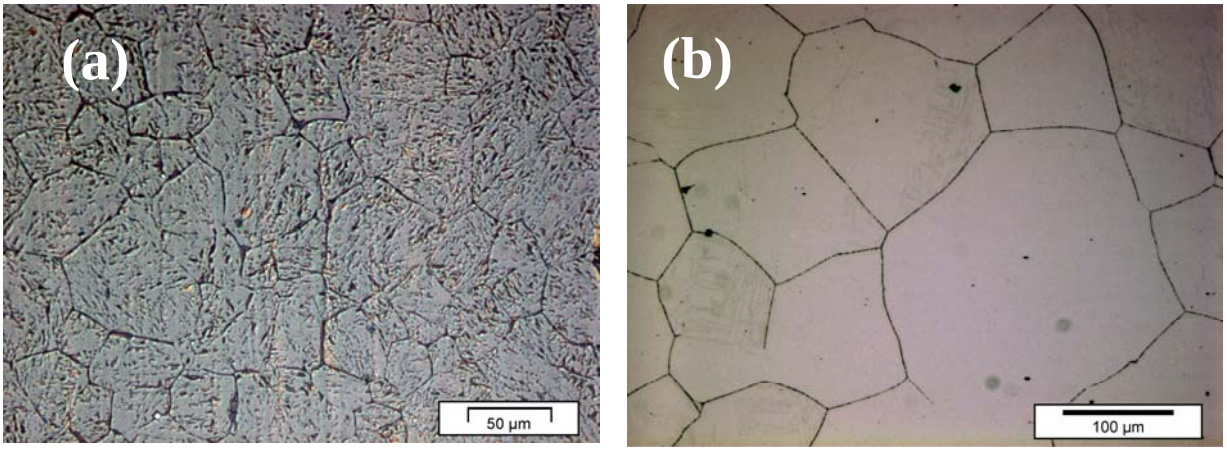


Figure 1 Optical micrographs of specimen after homogenisation treatment at 1100 $^{o}$C for a) 300 s and b) 1800 s

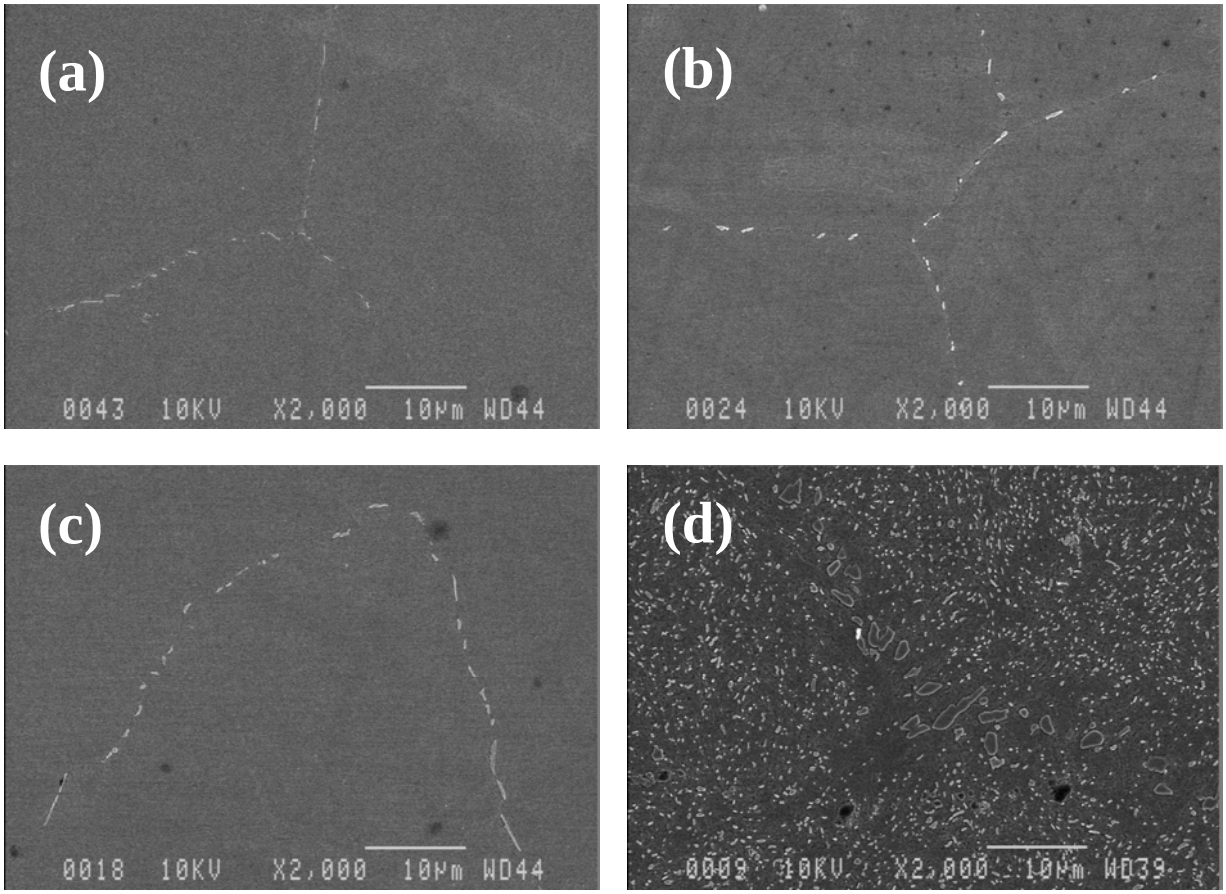


Figure 2 Scanning electron micrographs of specimens homogenised at 1100 $^{o}$C for 1800 s and aged at 900 $^{o}$C for (a) 300 s, (b) 1800 s, (c) 3600 s and (d) 50400 s.

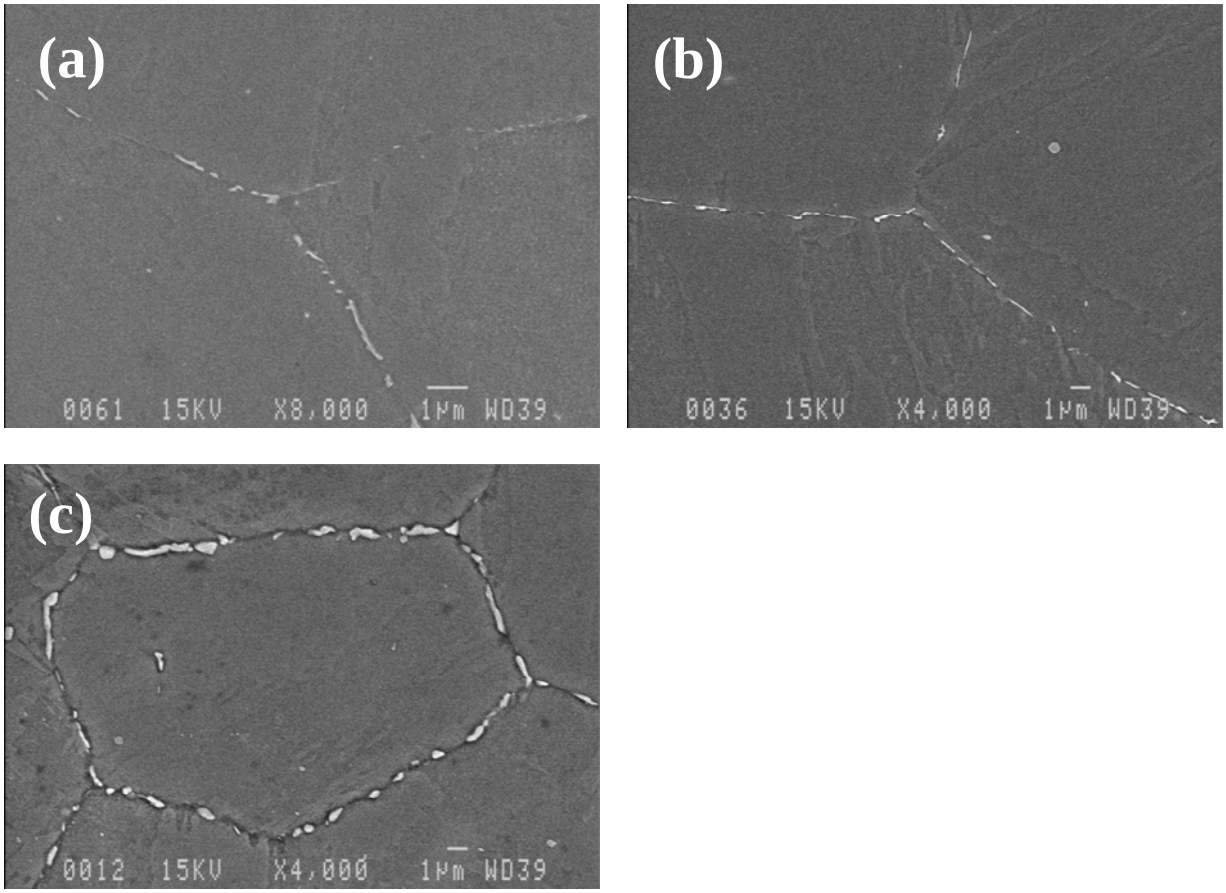


Figure 3 Scanning electron micrographs of specimens homogenised at 1100 $^{o}$C for 300 s and aged at 900 $^{o}$C for (a) 300 s, (b) 1800 s and (c) 3600 s.

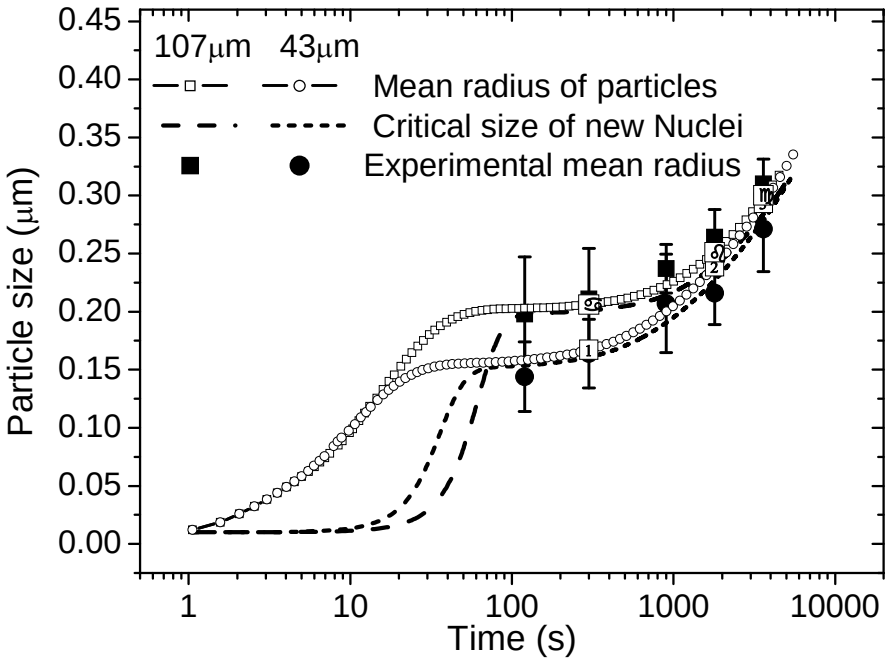


Figure 4 Predicted and experimental evolution of Chi precipitate average and critical radius as a function of time at 900 $^{o}$C for the average austenite grain size 107 μm (square) and 43 μm (circle), homogenisation pre-heat treated at 1100 $^{o}$C for 1800 s and 300 s, respectively.

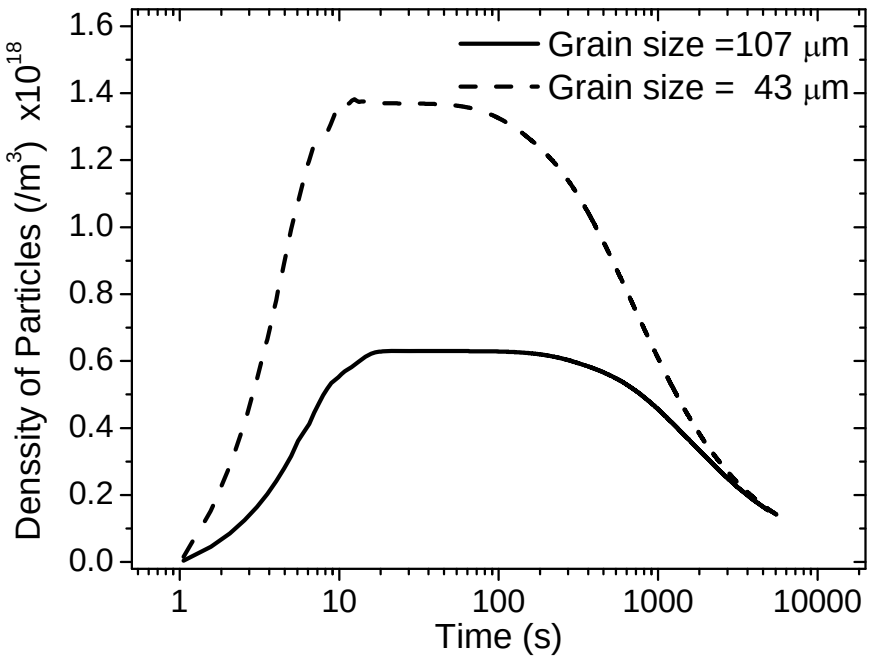


Figure 5 Predicted evolution of density of Chi precipitate particles as a function of time at 900 $^{o}$C, for two average austenite grain size 107 μm and 43 μm.

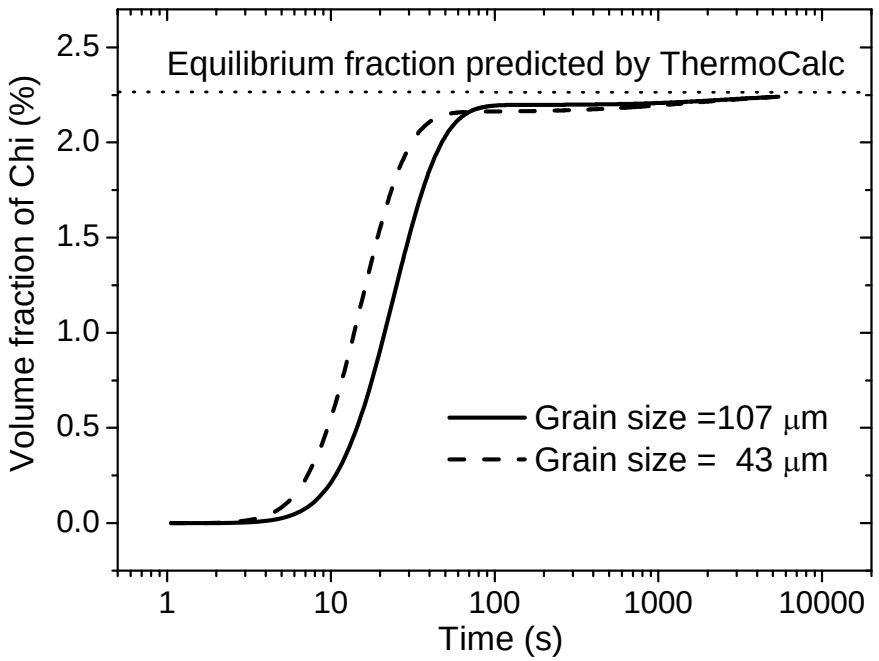


Figure 6 Predicted evolution of volume fraction of Chi precipitate as a function of time at 900 $^{o}$C, for two average austenite grain size 107 μm and 43 μm.

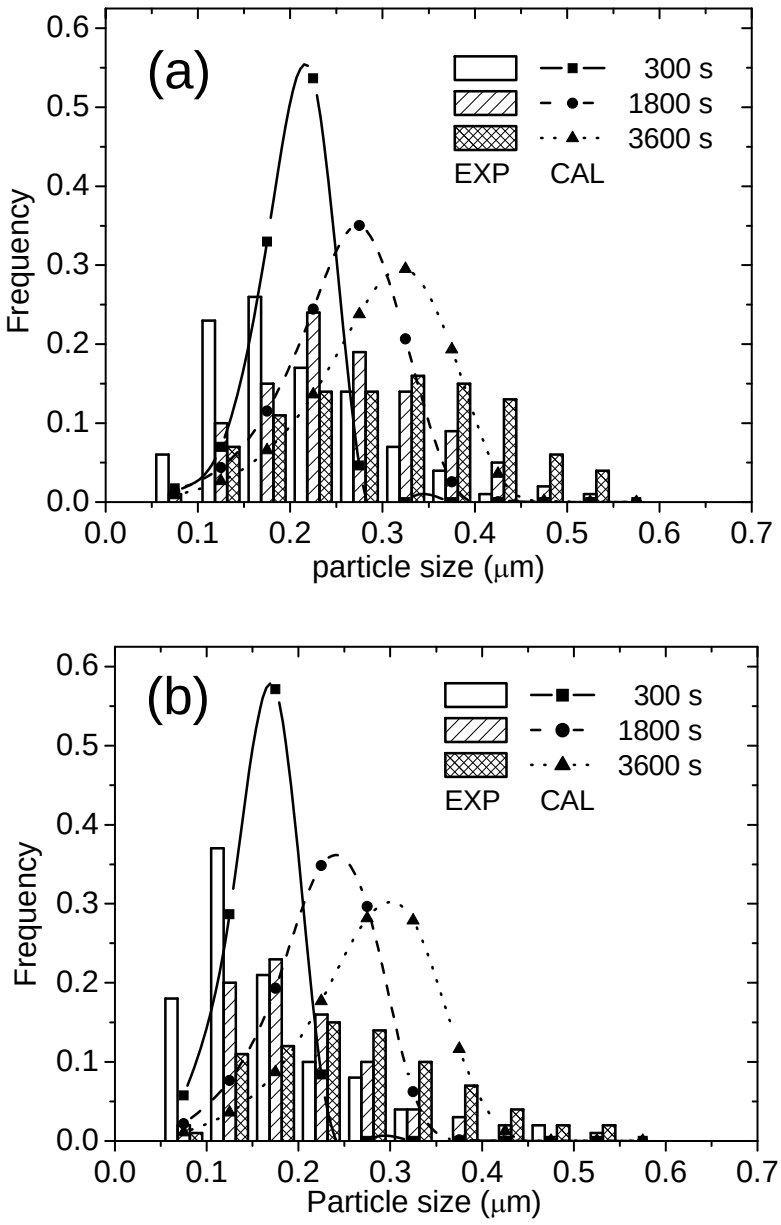


Figure 7 Predicted and experimental results of particle size distribution of Chi precipitate for 300 s, 1800 s and 3600 s ageing at 900 $^{o}$C, for two average austenite grain size (a) 107 μm and (b) 43 μm, homogenisation pre-heat treated at 1100 $^{o}$C for 1800 s and 300 s, respectively.